Advances in Water Resources 218 (2026) 105531

Contents lists available at ScienceDirect

Advances in Water Resources

journal homepage: www.elsevier.com/locate/advwatres

A multiscale digital-rock workflow for shale-matrix flow characterization: Application to permeability prediction

Zhiwei Wang [a,b,d], Jianqi Rong [a,b], Bowen Shi [a,b], Dongchen Liu [c], Yingfang Zhou [d], S. Majid Hassanizadeh [a,b,e], Yongfei Yang [f], Chao-Zhong Qin [a,b,*]

[a] School of Resources and Safety Engineering, Chongqing University, Chongqing, China
[b] State Key Laboratory of Coal Mine Disaster Dynamics and Control, Chongqing University, Chongqing, China
[c] Shale Gas Research Institute, PetroChina Southwest Oil & Gas field Company, Chengdu, Sichuan Province, China
[d] School of Engineering, University of Aberdeen, Aberdeen, United Kingdom
[e] Department of Earth Sciences, University of Utrecht, Utrecht, the Netherlands
[f] State Key Laboratory of Deep Oil and Gas, China University of Petroleum (East China), Qingdao, China

ARTICLE INFO

Keywords:
Digital rocks reconstruction
Shale matrix
Pore connectivity
Apparent permeability
Multiscale pore-network model
SliceGAN

ABSTRACT

Besides gas production, shale reservoirs can be of great interest to geological carbon storage and underground hydrogen storage. Characterizing shale-matrix flow properties is important for these applications. In particular, shale-matrix permeability is one of the most important flow properties. However, predicting permeability is challenging because shale-matrix pore structures span multiple scales that cannot be captured by a single imaging technique. Our imaging techniques suffer from an inherent trade-off between spatial resolution and field of view. To bridge this gap, we develop a shale-specific multiscale digital-rock workflow that integrates high-resolution two-dimensional pore-scale information with large-area mineral and organic-matter images to construct three-dimensional shale-matrix models at Representative Elementary Volume (REV) scale. First, pore-bearing regions are classified into three sub-rock types: two organic-matter types, distinguished by the connectivity of their wettability and resolved pores and one clay-associated type. Porosity and permeability values for each type are quantified using MAPS and FIB-SEM (Focused Ion Beam–Scanning Electron Microscopy) imaging combined with pore-scale modelling. These are then assigned to corresponding three-dimensional REV-scale regions generated using SliceGAN. The workflow thereby incorporates high-resolution pore information through local properties while representing the larger-scale spatial arrangement and connectivity of pore-bearing region at the REV scale. We applied this workflow to twelve shale samples and determined their pore connectivity and apparent gas permeabilities. We also measured permeabilities of each shale sample experimentally. The predicted permeability values agree well with experimental measurements. Our results reveal that shale matrix permeability reflects the combined influence of local flow properties, relative abundance, and spatial connectivity of the sub-rock types. We also find that mixed-facies shales exhibit higher average permeability than siliceous shales despite their lower organic-matter content, owing to more abundant and spatially connected clay-associated regions that link otherwise separated organic-matter domains. To the best of our knowledge, this is a novel workflow for constructing digital rocks of shale matrix and determining flow and transport properties of shale, with its application to apparent gas permeability assessed against experimental measurements. It can be extended to other flow properties, including relative permeability–saturation and capillary pressure–saturation relationships.

1. Introduction

Shale formations can play a dual strategic role in the global energy transition, i.e., acting as primary reservoirs for unconventional hydrocarbons (shale oil and gas), and providing critical sites for geological CO_2 sequestration and underground hydrogen storage (Ma et al., 2021; Wang et al., 2024a, b). Establishing a deep understanding of pore connectivity within shale matrix and its influence on

* Corresponding author at: State Key Laboratory of Coal Mine Disaster Dynamics and Control, Chongqing University, Chongqing, 400044, China.
E-mail address: chaozhong.qin@cqu.edu.cn (C.-Z. Qin).

https://doi.org/10.1016/j.advwatres.2026.105531
Received 10 August 2026; Received in revised form 6 October 2026; Accepted 11 October 2026
Available online 13 October 2026
0309-1708/© 2026 Elsevier Ltd. All rights are reserved, including those for text and data mining, AI training, and similar technologies.

permeability is paramount for optimizing unconventional resource extraction and for reliably assessing the long-term containment security and injection feasibility of geological storage projects (Chen et al., 2023; Alafnan, 2024; Wang et al., 2024a). Shale matrix, however, is characterized by multimineral composition and extreme pore heterogeneity (Loucks et al., 2012; Gao et al., 2024), which impose challenges in the study of shale pore connectivity and permeability.

Over the past few years, a variety of imaging and data-driven approaches have been developed to characterize and reconstruct the multiscale pore structure of shale. Focused Ion Beam–Scanning Electron Microscopy (FIB-SEM) enables high-resolution three-dimensional characterization of pores in organic matter (OM) and clay minerals at the tens- to hundreds-of-nanometers scale (Ma et al., 2018; Wei et al., 2023; Qin et al., 2024). However, its imaging volume is typically limited to only a few cubic micrometers, which is far smaller than the Representative Elementary Volume (REV) of shale matrix (Ma et al., 2019; Fan et al., 2022, 2023). Nano-Computed Tomography (Nano-CT) provides a larger field of view, typically from tens to hundreds of micrometers, but its spatial resolution is insufficient to resolve many nanoscale pores in OM and clay minerals (Wang et al., 2016; Gou et al., 2019; Li et al., 2021, 2024). Micro-CT further extends the observation scale to the millimeter-to-centimeter range, but mainly resolves micron-scale pores and fractures (Wang et al., 2020). In parallel, machine-learning-based approaches have been increasingly used for shale image reconstruction. Super-resolution methods can enhance image resolution, but their ability to bridge very large-scale gaps remains limited, particularly when nanoscale information must be recovered from much coarser observations (Wu et al., 2023a; Chen et al., 2025). GAN- and SliceGAN-based methods can reconstruct three-dimensional pore structures, but the generated structures are still primarily constrained by the scale and resolution represented in the training images (Kench and Cooper, 2021; Zhang et al., 2021; Zhao et al., 2021; Kench et al., 2022). For example, GAN reconstruction based on nano-CT images is limited to pores resolvable at the nano-CT scale, while SliceGAN-based reconstruction from high-resolution SEM images does not inherently integrate such fine-scale pore information with larger-scale mineral and organic-matter distributions. Therefore, existing approaches either resolve fine pore structures over domains smaller than the shale-matrix REV, or reach representative scales without retaining sufficient tens-of-nanometers pore-structure information.

On the other hand, There have been several numerical studies of shale matrix permeability. Cao et al. (2019) developed a pore-network model to simulate the permeability of different OM types. To consider sub-resolution pores in a FIB-SEM image of OM, Liu et al. (2025a) employed a hybrid pore-network-continuum model to predict the permeability and gas production behaviors of various OM types. However, their simulations were only for OM, making it difficult to represent the overall permeability of shale matrix. Guo et al. (2018) incorporated gas transport processes in different shale components, including OM, clay minerals, and macropores, into a micro-continuum numerical framework. Based on FIB-SEM images with a domain size of 3.56 μm × 2.50 μm × 3.36 μm, they simulated single-phase compressible methane flow in shale digital rocks. However, such micrometer-scale FIB-SEM domains were insufficient to reach the REV of shale due to its strong heterogeneity. Feng et al. (2024) constructed shale pore structures by numerically prescribing pore connectivity through assigned coordination numbers and connections between neighboring pores within a regular cubic lattice, and used these structures to simulate gas transport and permeability in the shale matrix. However, the pore connectivity was numerically imposed rather than directly extracted from real shale geometries, so the representativeness of such generated structures remains uncertain.

To address the inherent trade-off between spatial resolution and field of view in the characterization of shale matrix, we develop a multiscale digital-rock workflow for shale-matrix flow characterization. The workflow integrates high-resolution pore information with larger-area distributions of organic matter and clay minerals, using SliceGAN to construct three-dimensional shale-matrix models. Its methodological contribution lies in combining connectivity-based sub-rock classification, multiscale image integration, and the assignment of locally determined flow properties to the reconstructed matrix. This enables predictions. This enables fine-scale pore characteristics to influence larger-scale flow prediction without explicitly resolving all pores throughout the reconstructed domain. Using twelve subsurface shale samples, we assess the workflow through comparisons between predicted and measured apparent gas permeabilities and investigate how local flow properties, sub-rock abundance, and spatial connectivity jointly influence shale-matrix permeability. Although demonstrated here for apparent gas permeability, the workflow provides a basis for investigating additional flow properties (e.g., gas relative permeability) through further model development and validation.

2. Materials and methods

2.1. Overview of the multiscale workflow

The workflow comprises three interconnected stages (Fig. 1). First, high-resolution MAPS images are segmented and analyzed using a watershed-based procedure to identify organic-matter regions. These are classified into two sub-rock types according to the connectivity of their resolved pores: OM-A, with connected resolved pores, and OM-B, with disconnected resolved pores. Clay-associated regions constitute the third sub-rock type and are identified using QEMSCAN mineral maps.

Second, the classified organic-matter distributions are coarsened and combined with the corresponding clay distributions to produce composite images that retain the identities and spatial arrangement of the sub-rock types. These images provide the input for SliceGAN-based construction of three-dimensional shale-matrix models at the target REV scale.

Third, fine-scale imaging and numerical flow simulations are used to establish porosity and permeability descriptions for the sub-rock types. Local porosities and the corresponding intrinsic and apparent gas permeabilities are assigned to regions of the reconstructed matrix. The resulting models are used to analyse connectivity and calculate matrix-scale apparent gas permeability, which is compared with experimental measurements. Fine-scale pore information is thus incorporated through local properties, while the larger-scale reconstruction represents the spatial arrangement and connectivity of the pore-bearing regions.

2.2. Multiple imaging of shale matrix

Details of the shale samples, including sampling depths, geological setting, and mineralogical compositions, are provided in Appendix B. For multiscale characterization, the shale samples were analyzed using MAPS, QEMSCAN, and FIB-SEM. A cubic block sample of 1 cm × 1 cm × 0.5 cm was cut from each shale core. After mechanical polishing, the samples were further refined using argon ion polishing to produce a smooth surface. To enhance electrical conductivity and improve image quality, a thin carbon coating was applied to the whole sample. Large-area SEM mosaic images were acquired using MAPS on a Zeiss Crossbeam 540 microscope at 16 nm resolution with 12288^2 pixels, covering a 196.6 μm field of view (Wu et al., 2023a, b). Following SEM imaging, mineralogical composition was quantitatively analyzed using QEMSCAN. The resulting mineral maps covered an area of 450 μm × 3041 μm, with a resolution of 440 nm. This provided an image size of 1024×6912 pixels, and detailed mineral distribution information.

High-resolution 3D geometries of shale matrix were characterized using FIB-SEM with the ATLAS 3D module. Imaging sites were selected from OM sub-regions representing a range of surface porosities. Serial sectioning was conducted with a consistent slicing thickness and pixel

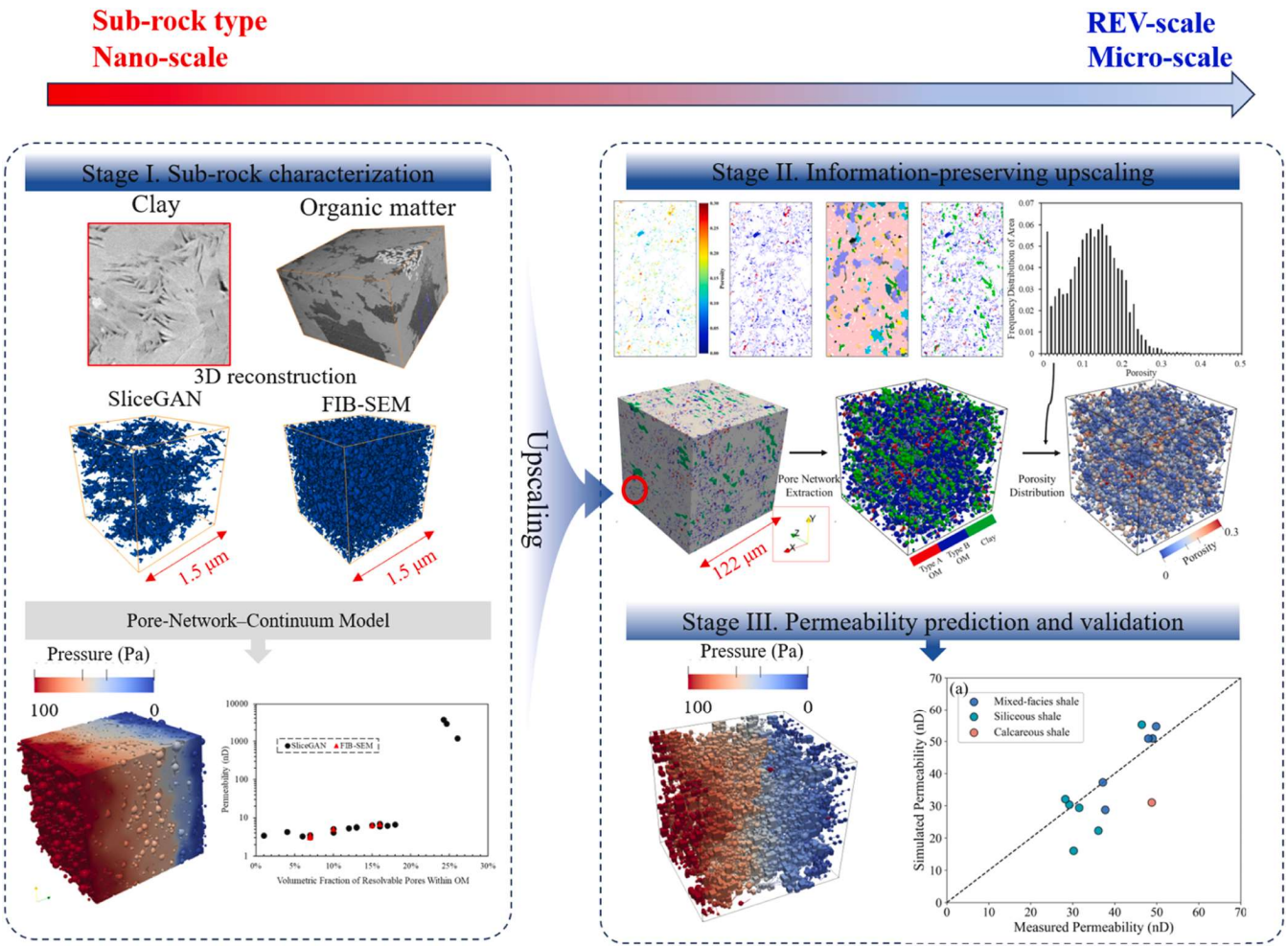


Fig. 1. Overview of the multiscale digital-rock workflow for shale-matrix flow characterization.

size of 4 nm. Detailed parameters for each imaging site, including component backgrounds and field of view, are summarized in Table S1 in the Supporting Information.

The shale samples were crushed and sieved to a particle size range of 10–12 mesh (1.7–2.0 mm in diameter) (Jiang et al., 2023). After drying at 110 °C and vacuum treatment, porosity and permeability were measured using the helium pressure-decay method. The permeability values used for comparison with the numerical predictions were obtained at an equilibrium pressure of approximately 0.7 MPa. Gas pressure variations between the reference and sample chambers were recorded, and pore volume and porosity were calculated based on the ideal gas law. Permeability was determined by fitting the pressure-decay curve under the assumption that the particles were ideal spheres following the gas-diffusion model (Cui et al., 2009; Jiang et al., 2023).

Combined results from QEMSCAN and MAPS analyses show that the areal fractions of OM and clay minerals correspond well with the bulk particle porosity obtained from quantitative porosity tests. As the contents of clay minerals and OM increase, the overall particle porosity of shale increases accordingly (Fig. 2), which is consistent with previous studies (Wang et al., 2019).

MAPS images indicate that the resolved pores in the shale matrix occur predominantly within organic matter (OM) and in association with inorganic clay minerals (as shown in Fig. 3). Dissolution pores in calcite or dolomite and other intergranular pores are relatively scarce and not connected to the global pore system (Ma et al., 2019). Therefore, their contribution to matrix-scale flow was assumed to be negligible. Accordingly, only clay minerals (along with their internal inorganic

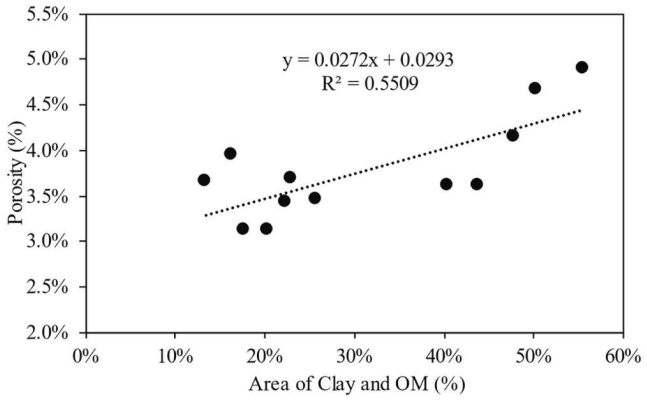


Fig. 2. Relationship between shale porosity and the combined proportions of clay minerals and OM.

pores) and OM (together with their OM pores) were represented in the REV-scale digital rock models. The clay mineral pores are mainly triangular or slit-shaped, while organic pores exhibit circular to elliptical morphologies with a broad size distribution ranging from several tens to several hundred nanometers. In contrast, the pore diameters within clay minerals are generally <100 nm (as shown in Fig. S1 in the Supplementary Information).

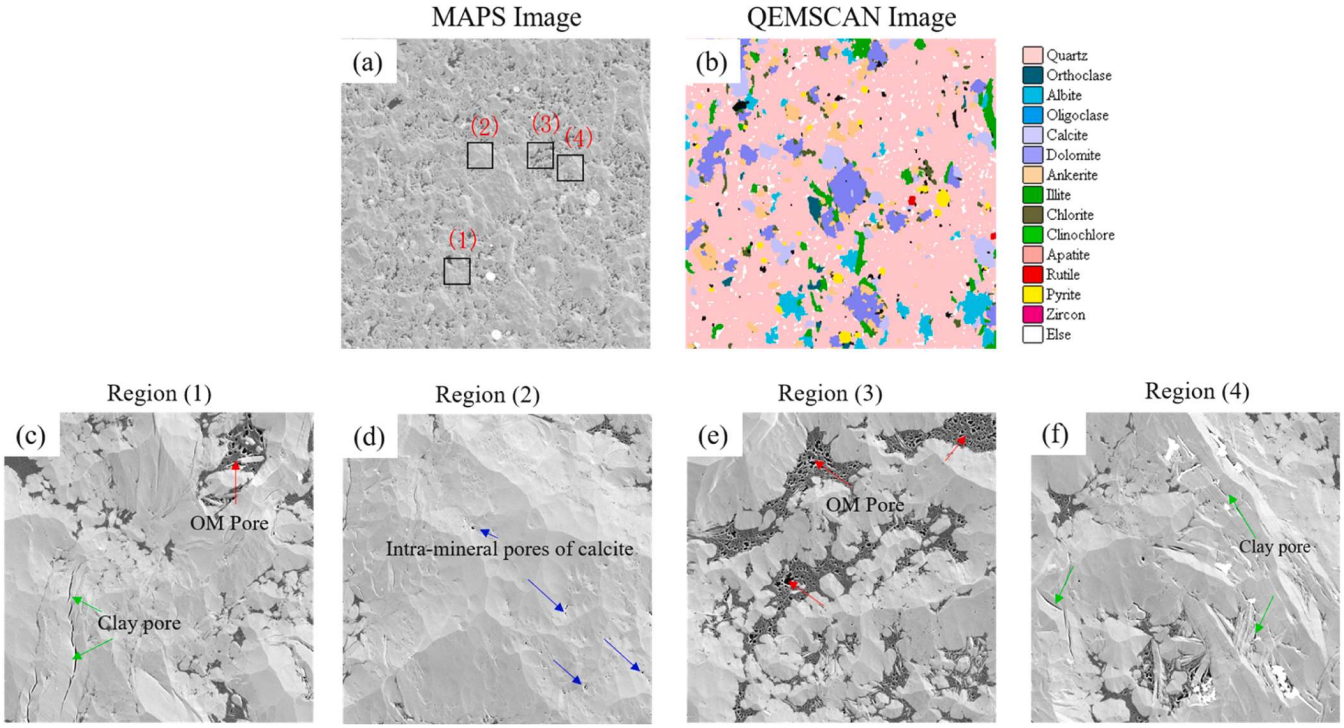


Fig. 3. Typical pore development characteristics of shale (Sample H9). (a) Large-area MAPS image showing the locations of four representative regions; (b) corresponding QEMSCAN mineral map; (c) Region (1), showing both OM pores and clay-associated pores; (d) Region (2), showing intra-mineral pores within calcite; (e) Region (3), showing abundant OM pores; and (f) Region(4), showing clay-associated pores.

2.3. Sub-rock typing of pore structures and 3D construction of shale matrix

To construct shale-matrix digital rocks at target REV scale while incorporating fine-scale pore information, we combined sub-rock classification with multiscale image integration and three-dimensional reconstruction. In this approach, pore-bearing regions are represented as sub-rock elements whose internal pore characteristics are incorporated through assigned local properties.

The high-resolution MAPS images were first processed in ImageJ using the Weka Segmentation plugin (Arganda-Carreras et al., 2017). Training images were manually labeled into four categories: OM, organic pores, inorganic pores, or solid minerals. After the classifier was trained, the 12,288×12,288-pixel mosaic, covering approximately 196.6 × 196.6 μm^2, was divided into 144 sub-images of 1024 × 1024 pixels, each covering approximately 16.38×16.38 μm^2, for automated segmentation. Previous studies utilizing spatial statistical analysis of shale mineral compositions have demonstrated that matrix mineral proportions tend to stabilize when the observation scale reaches approximately 100 μm, signifying that the REV has been attained (Liu et al., 2025b).

Following Liu et al. (2025b), the segmented organic pores were combined with the OM phase to define the boundaries of pore-bearing OM regions. A watershed algorithm (Beucher and Lantuéjoul, 1979) was then applied to subdivide the OM phase into individual elements. For each element, the resolved areal porosity was calculated as the area occupied by resolved organic pores divided by the total area of the element, including its pores (Fig. 4).

The OM elements were classified into two sub-rock types using resolved areal porosity as a proxy for internal pore connectivity. Elements with porosities above approximately 20% were assigned to OM-A, associated with connected resolved pores, whereas the remaining

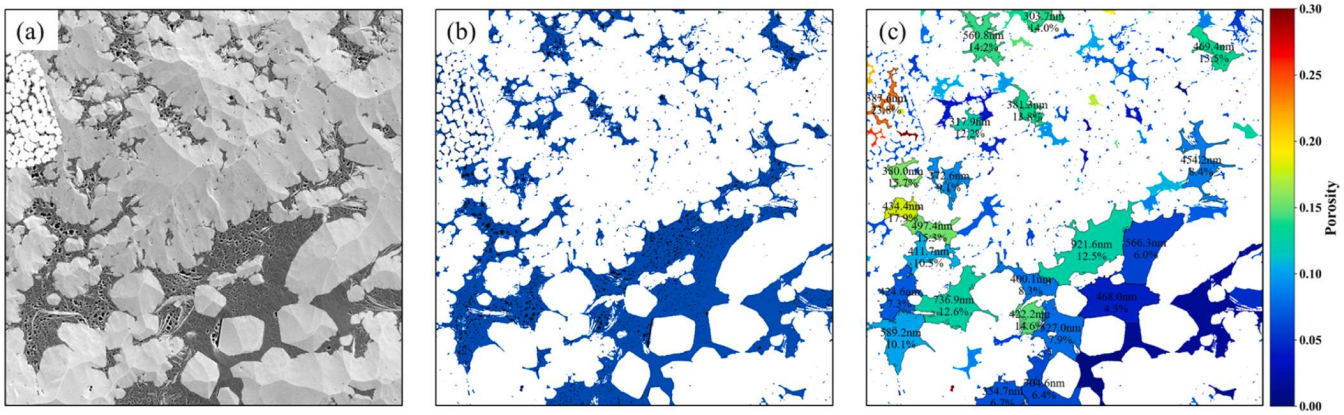


Fig. 4. Schematic of OM surface porosity and size analysis (Sample H9 in Table 1). (a) Part of the MAPS image; (b) segmented image; (c) watershed-segmented image showing individual OM elements, where the size, surface porosity, and average internal pore diameter of each watershed are calculated.

elements were assigned to OM-B, associated with disconnected resolved pores. The fine-scale connectivity and flow analyses supporting this classification are presented in Section 2.3. Clay-associated regions constituted the third sub-rock type.

To combine the organic-matter and mineral distributions, the classified MAPS images were coarsened from the original pixel size of 16 nm to a common pixel size of 320 nm, corresponding to a 20 × 20 pixel block. The QEMSCAN mineral maps, which have a coarser native spatial resolution of 440 nm, were resampled onto the same 320 nm computational grid. This common grid facilitates the integration of the two datasets while avoiding unnecessary computational cost associated with retaining the original 16 nm MAPS resolution. Because clay-associated regions could not be reliably distinguished from the MAPS images alone, their locations were obtained from the corresponding QEMSCAN maps. The two datasets were then overlaid to produce composite images representing the spatial distributions of OM-A, OM-B, and clay-associated regions (Fig. 5).

Finally, the composite images were used as input to SliceGAN to generate three-dimensional shale-matrix models (Fig. A1). SliceGAN consists of a three-dimensional generator and three two-dimensional discriminators operating on orthogonal slices, enabling the generated volume to reproduce the structural characteristics of the input two-dimensional images along the three principal directions. Each reconstructed volume comprised 382 × 382 × 382 voxels. At the adopted voxel size of 320 nm, this corresponds to a physical side length of approximately 122 μm. Previous spatial statistical analyses indicate that shale mineral proportions tend to stabilize at observation scales of approximately 100 μm, providing a compositional basis for selecting this reconstruction domain

Networks representing the connections among the reconstructed OM-A, OM-B and clay-associated elements were subsequently extracted to quantify matrix-scale connectivity. To incorporate local porosity information into the reconstructed three-dimensional structure, the resolved-pore porosity of each OM watershed was first calculated from the MAPS images to obtain the corresponding two-dimensional porosity probability distribution. After reconstruction of the three-dimensional shale-matrix structure, porosity values were randomly sampled from this image-derived probability distribution and assigned to the corresponding 3D OM elements. Thus, the reconstructed structure determines the spatial arrangement and connectivity of the OM elements, whereas the mapping procedure preserves the statistical distribution of local porosity obtained from the high-resolution MAPS observations (see Fig. 5h).

2.4. Empirical equations for OM and clay permeability

Based on the multiscale characterization and construction results described above, this section details the numerical simulation framework used to determine the apparent permeability of the shale matrix. To simulate permeability of constructed REV-size digital rocks of shale matrix (e.g., Fig. 5h), we need to predescribe intrinsic and apparent permeability of OM and clay elements. Therefore, we need to develop their empirical equations. Representative OM and clay elements reconstructed from SliceGAN and FIB-SEM images were used to perform permeability simulations. Compressible flow in multiscale OM and clay elements was modeled by our in-house pore-network-continuum model (Shi et al., 2024, 2025; Liu et al., 2025a). In this model, resolved pores (i.e., resolved organic or inorganic pores) are represented by a pore network, while sub-resolution pores are treated as a continuum. The detailed computational procedures are provided in Shi et al. (2024) and

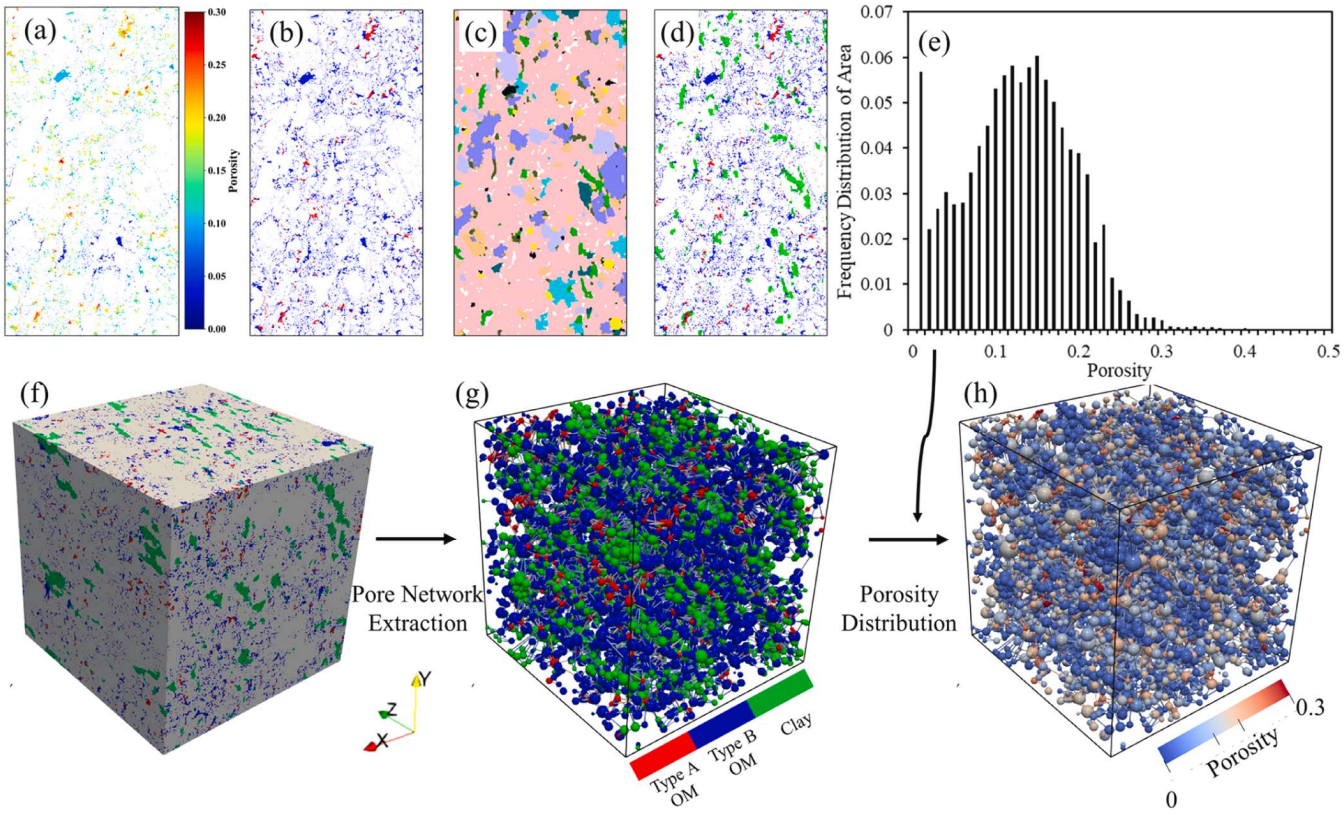


Fig. 5. Workflow for constructing REV-size digital rocks by integrating multi-source information (taking Sample H9 as an example). (a) porosity distribution of OM watersheds in the MAPS image; (b) classification and coarsening of OM watersheds; (c) clay mineral distribution of the same region acquired from QEMSCAN; (d) overlay of the classified OM with clay minerals to produce the combined distribution of OM and clay elements; (e) quantitative analysis of surface porosities of classified OM elements; (f) 3D construction of digital rock from the composite 2D image (d) using the SliceGAN with the size of 3823 voxels; (g) extraction of the pore network; (h) porosity distribution of OM and clay elements.

Liu et al. (2025a). Table 1 lists the geometrical and physical parameters used in our numerical simulations.

To determine intrinsic permeabilities of OM elements with varying porosities, sub-volumes of 382^3 voxels were extracted from the FIB-SEM images. Owing to scarce FIB-SEM data, additional 3D construction by SliceGAN was performed for 2D OM and clay watersheds with different surface porosities in the MAPS images. In total, 20 OM elements and 5 clay elements were constructed by SliceGAN, and 5 OM elements were from FIB-SEM reconstruction. Detailed structural parameters of the 3D OM and clay elements are provided in the Supplementary Information.

As shown in Fig. 6a, for OM elements, when porosity of resolved pores within OM is below 20%, these resolved pores remain disconnected. Intrinsic permeabilities exhibit linear dependence on porosity ranging from 3.33 nD to 6.97 nD. When porosities exceed approximately 20%, permeabilities rise sharply by nearly two orders of magnitude to the values between 1195.92 nD and 3679.01 nD. In contrast, clay elements generally exhibit porosities below 5%, with corresponding permeabilities between 1.32 nD and 1.65 nD. A comprehensive summary of porosity and permeability data for the simulated OM and clay elements is given in Table S2 in the Supporting Information. Additionally, 3D connectivity analysis was performed. For the OM elements, resolved pores in OM become fully interconnected along X, Y, and Z directions when porosities reach approximately 20%, while inorganic pores in clay elements are disconnected with low porosities. Fig. 7 shows the MAPS images, segmentation of resolved organic and inorganic pores, 3D construction by SliceGAN, and simulated flow fields by the pore-network-continuum model for four typical OM and clay elements.

Based on the above analysis, the OM watersheds or elements with surface porosities above 20% are classified as OM-A, while the rest are classified as OM-B with disconnected resolved organic pores. As shown in Fig. 6, for simplicity, we further assume that OM-A elements have an average intrinsic permeability of 2585.82 nD, clay elements have an average intrinsic permeability of 1.49 nD, and intrinsic permeabilities of OM-B elements are approximated by $(23.59\varepsilon + 2.49)$ nD (ε is the porosity of resolved organic pores).

The different permeability representations reflect the distinct transport characteristics of the three sub-rock types. For OM-B elements, intrinsic permeability varies systematically with resolved-pore porosity; therefore, the fitted porosity-dependent relationship was retained. Clay elements exhibit a relatively narrow permeability range (1.32–1.65 nD) and were therefore represented by their average value. OM-A elements, in contrast, have exceeded the connectivity threshold and belong to a distinctly high-permeability regime. Because OM-A occupies only a small fraction of the REV-scale matrix, its internal permeability variation was simplified using the average value while retaining OM-A explicitly as a highly conductive sub-rock type.

The intrinsic permeabilities of OM and clay elements need to be further revised to consider slip effect. Apparent permeabilities of OM elements considering surface diffusion of methane are estimated by Guo et al. (2018):

Table 1
Geometric and physical parameters used in our numerical simulations.

Parameters	Values
Average sub-resolution pore diameter of clay	5.7 nm
Average sub-resolution pore diameter of OM	5.7 nm
sub-resolution porosity of clay	0.05
sub-resolution porosity of OM	0.1
Characteristic length of OM-A elements	1×10^{-7} m
Characteristic length of OM-B elements	8×10^{-9} m
Characteristic length of clay	8×10^{-9} m
sub-resolution permeability of clay	1.19 nD
sub-resolution permeability of OM	2.46 nD
Density of adsorbed gas (ρ^{ad})	400 kg/m^3
Langmuir coefficient (K)	4×10^{-8} 1/Pa
Maximum adsorption (n_{max}^{ad})	44.8 kg/m^3

$$k_{a,om} = \frac{1}{\rho^g}\mu^g D_s n_{ad}^{max}\frac{K}{(1+Kp^g)^2} + (1+\alpha_{om}Kn)\left(1+\frac{4Kn}{1+Kn}\right)K_{OM} \quad (1)$$

where ρ^g denotes the gas density, μ^g is the dynamic viscosity, D_s represents the surface diffusion coefficient ($D_s = 8.32\times10^{-9}$ m^2/s), The parameter α is a fitting coefficient defined by the expression $\alpha = 1.5172 \times \frac{2}{\pi}\tan^{-1}(2.5\mathrm{Kn}^{0.4})$, n_{ad}^{max} is the maximum adsorption capacity, K is the Langmuir adsorption constant, and p^g is the gas pressure. The Knudsen number Kn is defined as $Kn = \lambda/L$, where λ is the mean free path and L represents the characteristic length. Since natural shale formations are typically water-bearing, gas adsorption in clay is negligible (Zhang et al., 2012; Rexer et al., 2014; Guo et al., 2018). Apparent permeabilities of clay elements, $k_{a,clay}$, are estimated by:

$$k_{a,clay} = (1+\alpha_{clay}Kn)\left(1+\frac{4Kn}{1+Kn}\right)K_{clay} \quad (2)$$

$\alpha = 1.358 \times \frac{2}{\pi}\tan^{-1}(4.0\mathrm{Kn}^{0.4})$, as proposed by Beskok and Karniadakis (1999). Once permeabilities of OM and clay elements are obtained, a multiscale pore-network model illustrated in Fig. 8 was employed to numerically simulate the overall apparent permeability of constructed digital rocks of shale matrix. For the model detail, one can refer to Zhao et al. (2025).

3. Results and discussion

3.1. Pore connectivity of shale matrix

Image analysis shows that porosities of OM watersheds in the segmented MAPS images are generally below 30%. The siliceous shale samples exhibit a broader range of OM porosities and higher average porosity compared with the mixed shale samples. On average, the areal proportion of OM-A in all samples is low, ranging from 0.03% to 2.31% (mean, 0.60%), whereas OM-B accounts for 4.65% ~ 12.12% (mean, 7.85%). The clay mineral content ranges from 2.79% to 39.66%, with an average of 18.44%. To further evaluate the impact of mineralogical compositions on the spatial distribution of OM and clay elements, three representative samples including H4, H8, and H9 were selected for comparative analysis. The mixed shale sample H4 has relatively high clay content, and OM porosity (i.e., the porosity of resolved pores in OM) mainly falls below 0.2, dominated by OM-B. In contrast, the siliceous shale samples H8 and H9 exhibit similar contents of OM and clay minerals. However, sample H8 shows a higher proportion of OM-A (with porosity > 20%), as illustrated in Fig. 9. Overall, the siliceous shale samples exhibit the highest average porosity (10.27%) of OM elements followed by the calcareous shales (7.54%). The mixed-facies shale samples show the lowest (6.69%), which is consistent with previous research findings (Guo et al., 2017).

By the developed technique, REV-size digital rocks of twelve shale samples in Table B1 were constructed. Each digital rock of shale matrix includes OM-A, OM-B and clay elements. The opensource PoreSpy (Gostick et al., 2019) was used to extract pore networks of clay and both types of OM elements, thereby quantifying their spatial connectivity as illustrated in Fig. 10. Coordination numbers of each element type and among different element types were calculated listed in Table 2. The results show that the mixed shale samples, characterized by its high clay content, exhibit the highest average coordination number (10.94), followed by calcareous shale (8.02) and siliceous shale (6.37). This trend indicates that the coordination number increases with increasing clay and OM content, suggesting that higher abundances of clay minerals and OM are associated with improved pore connectivity.

Taking the mixed shale sample H4 as an example, the constructed digital core reveals a high clay content. The average coordination number of clay elements is 6.83, while that of disconnected OM elements is 2.72, resulting in an overall mean coordination number of 11.88. For siliceous shale samples H8 and H9, which exhibit similar clay

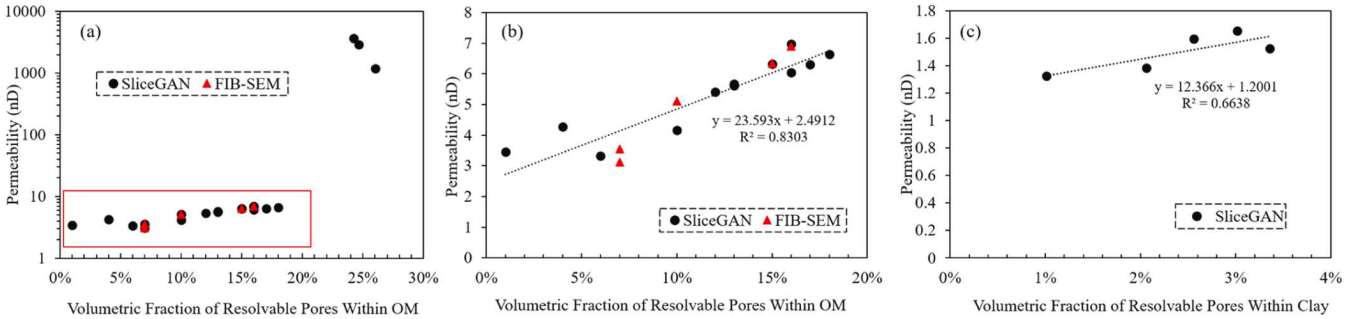


Fig. 6. (a) Relationship between porosities of resolved pores and permeability for OM elements. (b) Zoomed-in view of (a) showing the permeabilities with low porosities. (c) Relationship between porosities of resolved pores and permeability for clay elements.

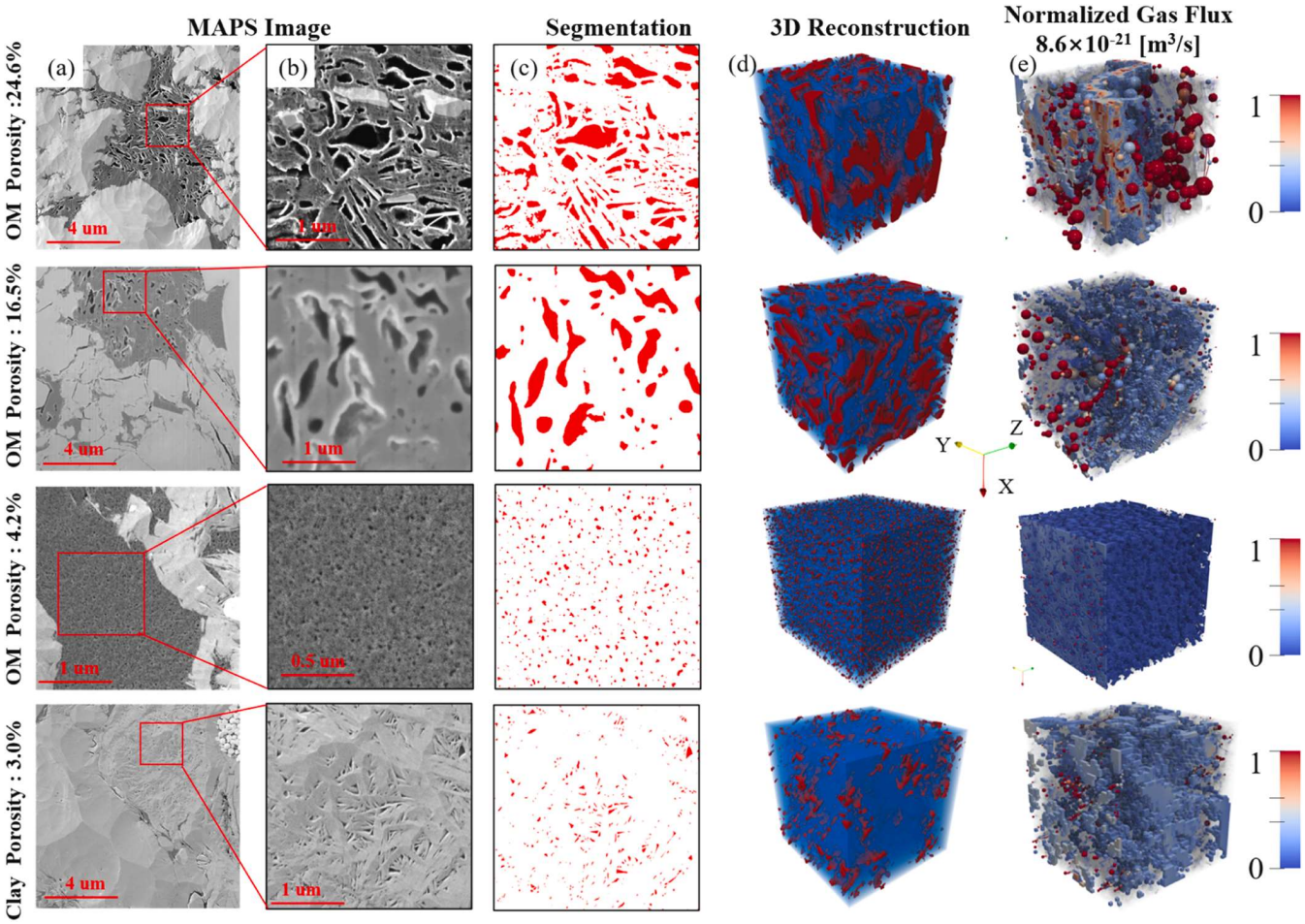


Fig. 7. Pore structure and connectivity characteristics of clay and OM elements at different porosities. (a) MAPS image; (b) enlarged view of (a); (c) pore segmentation of (b); (d) 3D pore constructions (rows 1, 3, and 4 from SliceGAN; row 2 from FIB-SEM); (e) flow field distribution by the pore-network-continuum model.

and OM contents, sample H8 contains a larger proportion of OM-A. However, due to its more uniform spatial distribution, its coordination number is lower than that of sample H9, where OM-A is more clustered. Overall, the coordination among OM-A, OM-B, and clay elements in sample H9 is higher than in sample H8.

REV-size digital rocks incorporating porosity information were generated as shown in Fig. 10. The results show that OM elements in the siliceous shale samples H8 and H9 exhibit significantly higher porosities than those in the mixed shale sample H4. Statistical analysis of the MAPS images reveals that OM surface porosities of the siliceous shale samples ranges from 0.61% to 16.04%, with an average of 8.19%. For the mixed-facies shale samples, OM surface porosities vary between 4.27% and 8.66%, averaging 6.63%. Additionally, the calcareous shale sample (H11) exhibits a lower OM porosity of 1.35%.

Connectivity analysis along the Z direction indicates that OM-A elements are universally isolated across all samples. Consequently, it must rely on OM-B and clay minerals to serve as structural bridges to establish global connectivity. The pore connectivity is heavily dictated by mineralogical variations and spatial distributions, leading to three distinct connectivity modes. The mixed shales exhibit a clay-dominated connectivity mode. For instance, in sample H4, despite the low coordination and lack of self-connectivity of OM-B elements, the high clay content (39.10%) enables the formation of an connected 3D pore network. This confirms that in mixed lithofacies, clay elements serve as

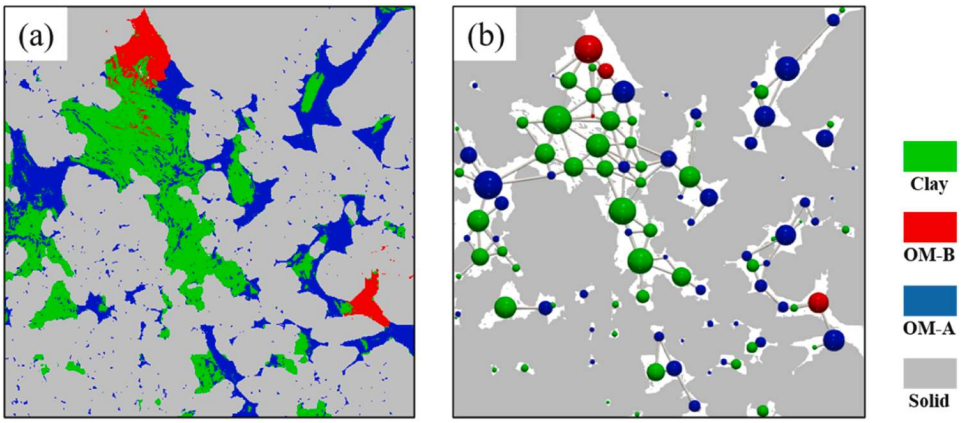


Fig. 8. 2D Schematic of the multiscale pore-network model. (a) spatial distribution of OM and clay. (b) Extraction of the multiscale pore network including OM-A, OM-B, and clay elements.

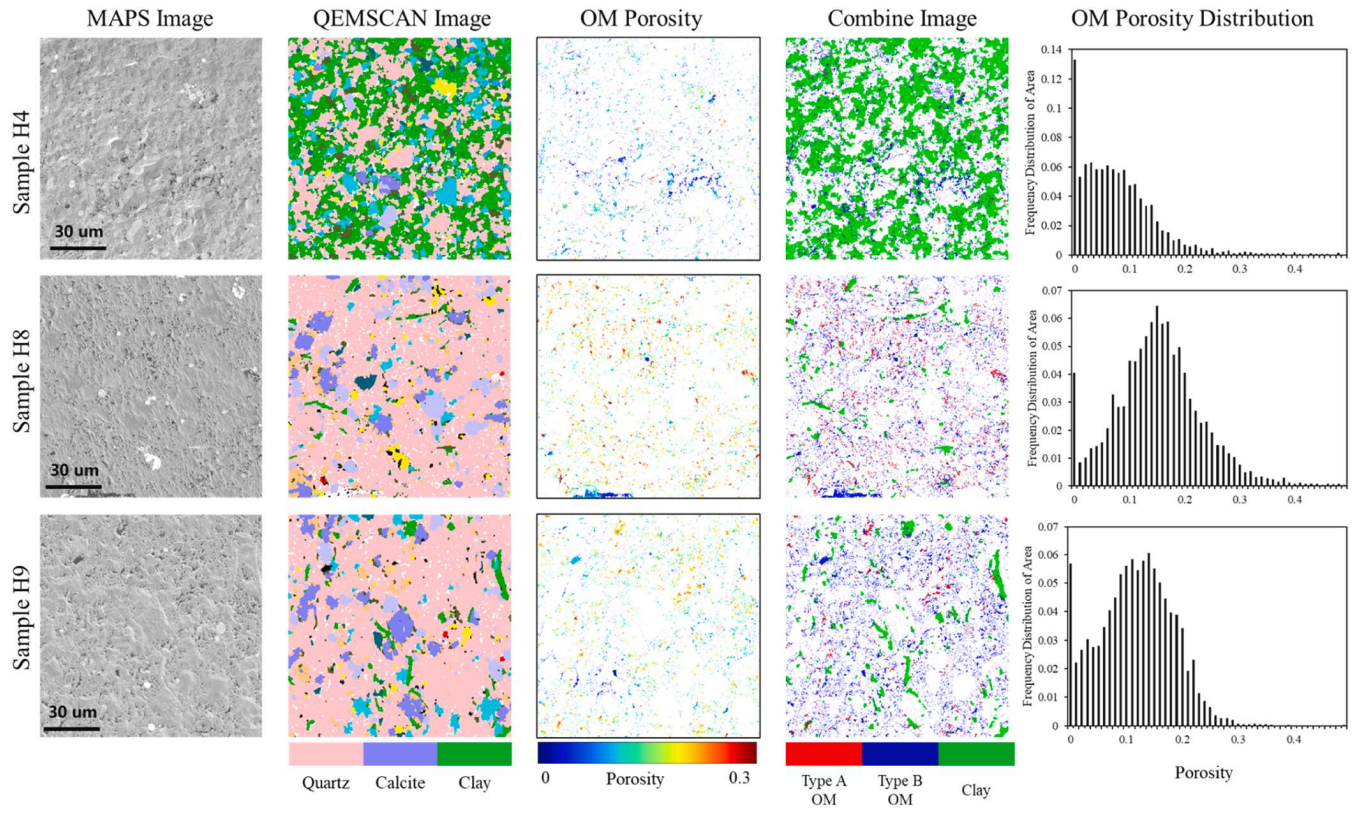


Fig. 9. Distribution of OM-A, OM-B, and clay elements in representative shale samples.

primary effective flow pathways. Secondly, the siliceous shales display a more complex synergistic connectivity mode. While OM networks are typically well-connected (with the exception of sample H12), the relatively low clay content often forces clay minerals to utilize OM as a bridge to integrate into the global network, as seen in samples H6, H8, and H9. Notably, in sample H8, no single component (OM-A, OM-B, or clay) can form an independent network throughout the domain, necessitating mutual interconnections to achieve overall pore connectivity. Finally, in the calcareous shale (sample H11) both OM and clay elements can form independent networks due to their moderate contents.

3.2. *Apparent permeability*

Permeability of shale matrix is a critical factor dictating the kinetics of gas absorption and transport, making the investigation of mineralogical controls essential. Using our in-house multiscale pore-network model (Zhao et al., 2025), the apparent permeabilities of the constructed digital shale matrix were numerically predicted under a gas pressure of 0.7 MPa. To drive the flow, a minor pressure gradient was applied while maintaining the mean gas-phase pressure at the experimental condition (0.7 MPa). As shown in Fig. 11a, the numerical values match the experimentally-measured permeabilities of shale particle samples well, confirming the reliability of the proposed framework for constructing realistic and REV-size digital rocks of shale matrix and predicting apparent permeability. The mixed-facies shales display the highest average permeability of 44.49 nD (ranging from 28.75 nD to 54.64 nD), followed by the calcareous shale (31.02 nD), and the siliceous shales which exhibit an average of 30.88 nD (ranging from 16.05

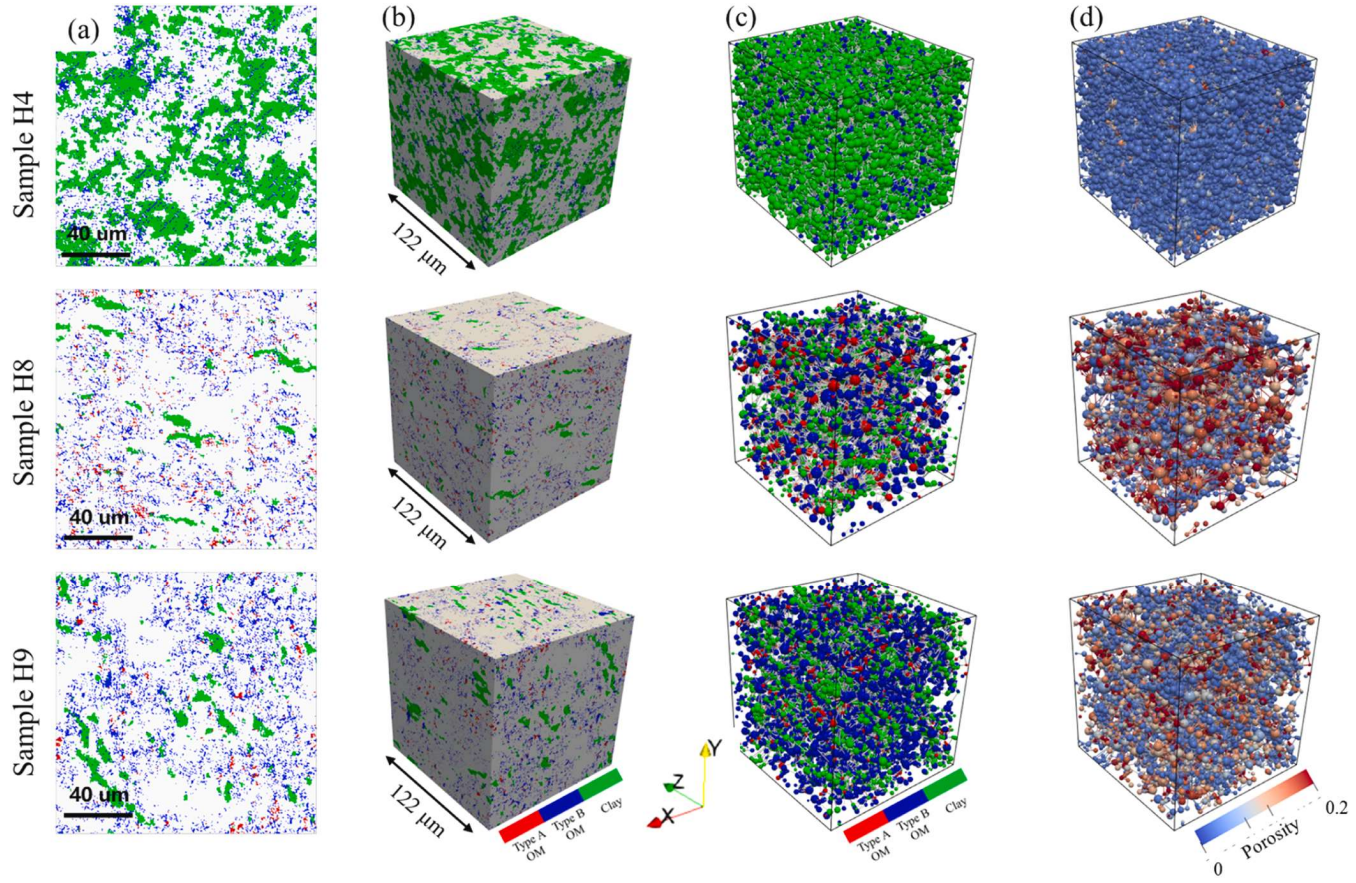


Fig. 10. REV-size digital rock construction of typical shale samples. (a) XY-plane slices of the 3D digital rocks generated by SliceGAN; (b) 3D rendering of the constructed digital rocks; (c) extracted pore networks of different element types; (d) porosity distributions of different element types.

Table 2
Proportions and coordination number statistics of different element types.

Sample	Lithofacies	OM-A			OM-B			Total OM	Clay			Total (REV)		
		CN	*f* (%)	*C*	*CN*	*f* (%)	*C*	*C*	*CN*	*f* (%)	*C*	*CN*	*f* (%)	*C*
H1	Mixed shale	—	—	×	3.52	5.1	×	×	6.22	26.4	✓	9.52	31.5	✓
H2	Mixed shale	0.1	0.6	×	2.84	5.9	✓	✓	6.74	32.3	✓	11.11	38.7	✓
H3	Mixed shale	—	—	×	6.66	8.3	×	×	6.31	30.1	✓	11.15	38.4	✓
H4	Mixed shale	—	—	×	2.72	7.3	×	×	6.83	39.1	✓	11.88	46.4	✓
H5	Mixed shale	—	—	×	2.2	6.3	×	×	6.48	37.2	✓	11.07	43.5	✓
H6	Siliceous shale	2.38	1.5	×	3.6	11.9	✓	✓	1.72	2.9	×	5.74	16.3	✓
H7	Siliceous shale	—	—	×	4.55	12.8	✓	✓	2.28	7.9	✓	6.89	20.7	✓
H8	Siliceous shale	0.99	2.5	×	1.64	7.1	×	✓	1.5	3	×	7.05	12.7	✓
H9	Siliceous shale	1.18	1.3	×	2.6	9.9	✓	✓	2.1	4.3	×	5.78	15.5	✓
H10	Siliceous shale	—	—	×	3.47	9.4	✓	✓	2.64	7.9	✓	5.7	17.3	✓
H11	Calcareous shale	—	—	×	2.66	7.5	✓	✓	2.96	14.5	✓	8.02	22.1	✓
H12	Siliceous shale	—	—	×	2.99	5.1	×	×	3.32	14.7	✓	7.1	19.8	✓

Notes:.
CN denotes the average coordination number of the elements.
f is the volume fraction (%) of each element within the REV.
C represents the Z-axis connectivity status obtained via Axis connectivity analysis; ✓ indicates a connected pathway, while × indicates isolated or disconnected elements.
The "Total (REV)" column accounts for the collective connectivity of all pore-bearing elements (OM-A, OM-B, and Clay).

nD to 55.18 nD), as shown in Fig. 11b. Within the shale matrix, this macroscopic flow capacity is predominantly governed by the topological connectivity of pore-bearing elements. Although the mixed-facies shales have a relatively low overall OM content, their high clay mineral abundance ensures superior pore-network connectivity, leading to higher permeability compared to the organic-rich but clay-poor siliceous shales.

Pressure distributions (Fig. 12) in H4 and H9 show uniform gradients, suggesting homogeneous flow resistance. In contrast, H8 displays rapid variations near boundaries and a smaller interior gradient, linked to its complex connectivity where high-resistance elements distort the local gradient. Mixed shale H4, clay and OM-B distributions largely overlap, suggesting balanced flow due to the clay scaffold. Conversely, the siliceous samples H8 and H9 show a clear hierarchy in pore-scale flow contribution: OM-A > OM-B > clay. Although H8 and H9 have comparable clay and total OM contents, H8 exhibits a

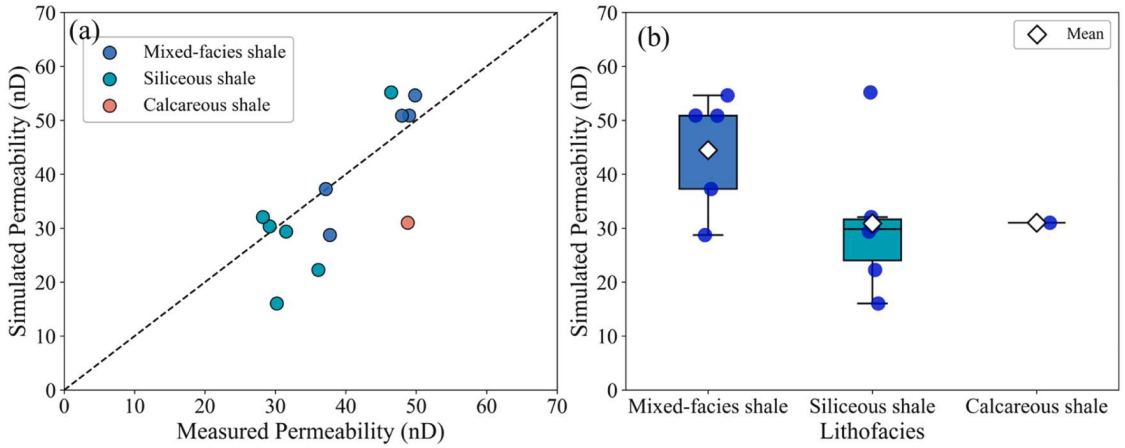


Fig. 11. (a) Comparison of the measured and simulated apparent permeabilities. (b) Distribution of simulated permeability across mixed-facies, siliceous, and calcareous shales.

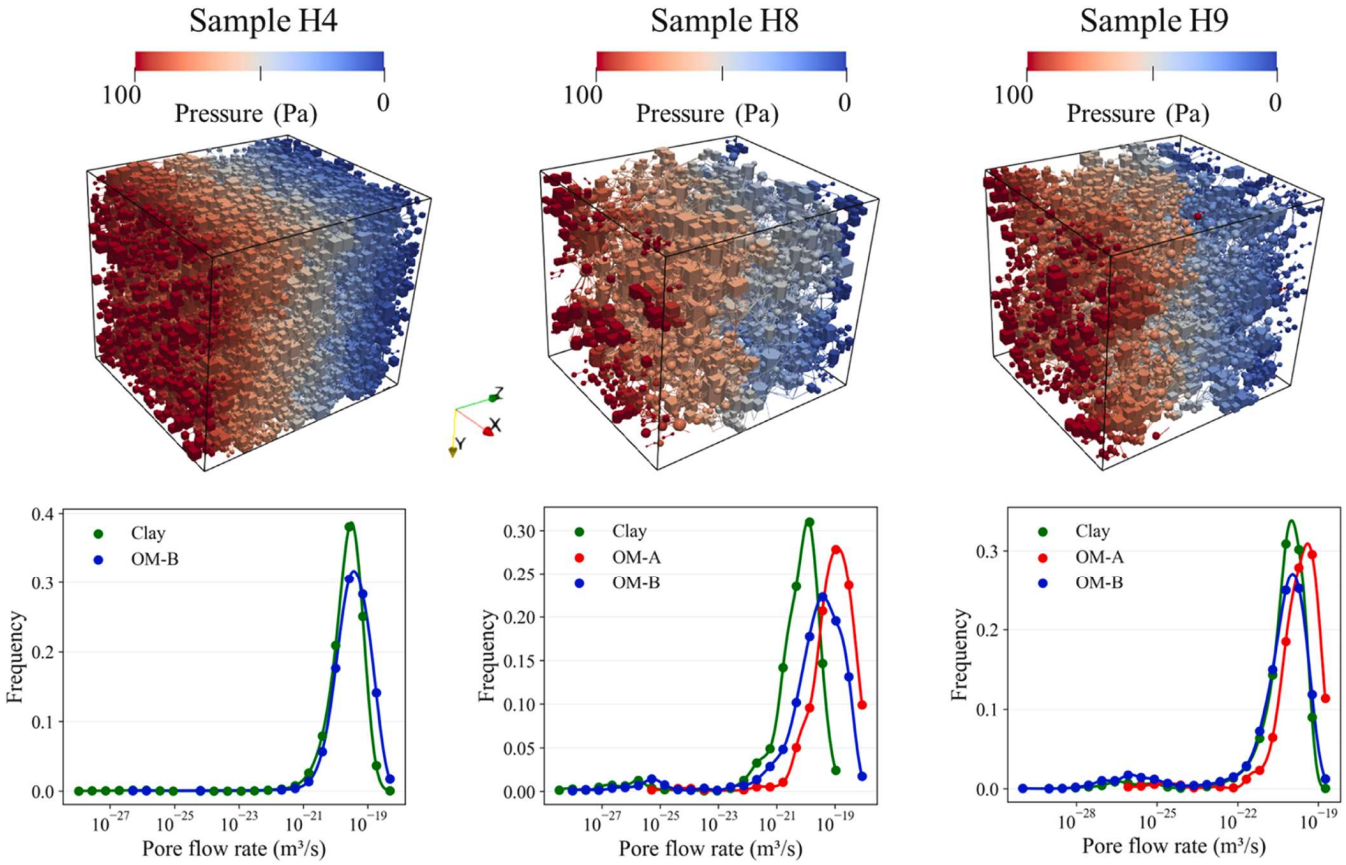


Fig. 12. Pressure fields (top) and pore-scale flow rate frequency distributions (bottom) for three typical shale samples. In the pore networks, rhombic prisms, spheres, and cubes represent OM-A, OM-B, and clay elements, respectively.

much higher permeability than H9, mainly because of its higher proportion of OM-A. This comparison demonstrates that classifying OM into OM-A and OM-B is essential; treating OM as a single phase would obscure the contribution of highly connected organic pores and lead to inaccuracies in permeability prediction.

Following these sub-rock scale flow insights, we further examined the REV-scale correlations between mineral composition and measured permeability. As shown in Fig. 13, permeability exhibits certain correlations with the contents of pore-bearing minerals, especially clay and total OM. However, these correlations are not strong, indicating that mineral abundance alone is insufficient to determine matrix permeability. Instead, permeability is also affected by the spatial distribution and connectivity of pore-bearing elements, as well as the relative proportions of OM-A and OM-B. This is further supported by the comparison between H8 and H9, which have similar clay and total OM contents but show markedly different permeabilities due to their different OM-A and OM-B proportions.

Based on the integration of REV scale connectivity analysis and permeability simulations, in mixed-facies shales, permeability is primarily clay-dominated, whereas in siliceous shales, transport capacity is

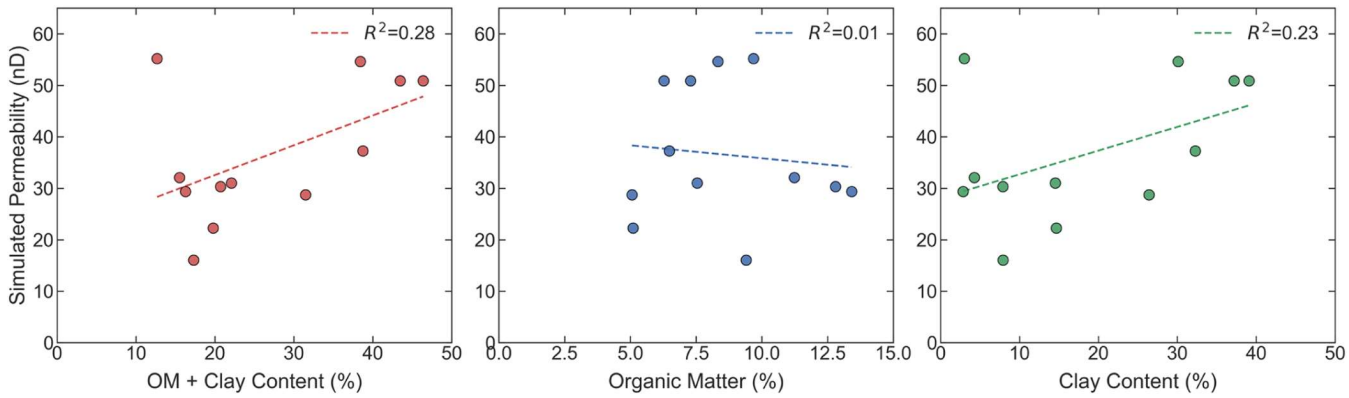


Fig. 13. Correlations between mineral composition and simulated permeability.

jointly governed by OM and clay. For samples with similar mineral contents, a higher proportion of OM-A significantly enhances the overall matrix permeability. Therefore, on the REV scale, permeability should be interpreted as the combined result of lithofacies/mineral composition, spatial distribution of pore-bearing elements, and OM-type heterogeneity. Notably, this study does not account for the influence of water content in either experiments or simulations. Given that transport patterns under moisture conditions may vary across different mineral compositions, investigating these effects remains a key direction for future research.

4. Conclusions

This study presents a multiscale digital-rock workflow for shale-matrix flow characterization. The workflow combines high-resolution pore imaging, classification of pore-bearing regions into two organic-matter types and one clay-associated type, integration of mineral and organic-matter distributions, and SliceGAN-based three-dimensional reconstruction. Fine-scale pore information is incorporated through local porosity and permeability assignments, allowing larger-scale flow calculations without explicitly resolving all pores throughout the reconstructed domain. The methodological contribution lies in integrating these steps to connect local pore characteristics with the spatial organization of the shale matrix.

Application to twelve shale samples demonstrates the workflow's ability to characterize connectivity among pore-bearing regions and predict apparent gas permeability, with predictions agreeing well with experimental measurements under the investigated conditions. The results lead to three main conclusions:

1. Connectivity within individual sub-rock elements and connectivity among those elements play distinct roles in matrix-scale flow. In the organic-matter elements analysed here, resolved pores become connected at porosities of approximately 20%, producing a marked increase in local permeability. However, these comparatively permeable OM-A elements do not independently form continuous pathways across the reconstructed matrices. Their contribution to matrix-scale flow therefore depends on connections through OM-B and clay-associated regions, whose local flow properties also reflect the contribution of sub-resolution pores.
2. Shale-matrix permeability depends jointly on the local flow properties, relative abundance, and spatial connectivity of the sub-rock types. Mixed-facies shales exhibit higher average permeability than siliceous shales in the investigated dataset, despite their lower organic-matter content. This behaviour is associated with the greater abundance and continuity of clay-associated regions, which connect otherwise separated organic-matter domains.
3. Mineral and organic-matter abundances alone are insufficient to explain permeability differences. Samples with similar overall compositions, such as H8 and H9, can exhibit different permeabilities because their organic matter differs in internal pore connectivity and in the relative abundance and spatial arrangement of highly permeable elements. Distinguishing OM-A from OM-B therefore provides information that is lost when organic matter is represented as a single uniform component.

These findings should be interpreted within the assumptions of the workflow. The sub-rock classification and local permeability descriptions were derived from a limited set of imaged and simulated elements; their applicability to other shale formations remains to be assessed. Sub-resolution pore properties are prescribed rather than fully resolved, and statistical porosity assignment does not necessarily preserve spatial correlations between local pore properties and surrounding mineral structures. Furthermore, three-dimensional reconstruction from two-dimensional images introduces uncertainty in connectivity and anisotropy. The selected domain size is supported by compositional representativeness, but convergence of connectivity and permeability with increasing domain size requires separate assessment. Agreement with the available measurements therefore supports the workflow under the investigated conditions, while further testing across domain sizes, reconstructed realizations, and experimental conditions is needed to establish its broader predictive reliability.

The reconstructed structures and property-assignment approach also provide a basis for investigating flow properties beyond apparent gas permeability. In particular, the workflow could be extended to calculate relative permeability–saturation and capillary pressure–saturation relationships by assigning appropriate multiphase constitutive descriptions to the sub-rock types and modelling fluid redistribution through their connected structure. Such extensions would require additional information on pore-throat geometry, wettability, interfacial tension, and fluid occupancy, together with appropriate treatment of displacement history and sub-resolution porosity. These properties cannot be inferred from the present single-phase permeability assignments alone. Their prediction would therefore require further model development and experimental validation, while retaining the central strategy of linking fine-scale characterization to larger-scale flow behavior.

CRediT authorship contribution statement

Zhiwei Wang: Writing – original draft, Visualization, Software, Methodology, Data curation, Conceptualization. **Jianqi Rong:** Validation, Software, Methodology. **Bowen Shi:** Visualization, Software, Formal analysis, Data curation. **Dongchen Liu:** Writing – review & editing, Supervision, Resources, Funding acquisition. **Yingfang Zhou:**

Writing – review & editing, Supervision, Methodology. **S. Majid Hassanizadeh:** Supervision, Writing – review & editing. **Yongfei Yang:** Supervision, Funding acquisition. **Chao-Zhong Qin:** Writing – review & editing, Supervision, Software, Resources, Data curation.

Declaration of competing interest

The authors declare that they have no known competing financial interests or personal relationships that could have appeared to influence the work reported in this paper.

Acknowledgments

We acknowledge the support of the National Natural Science Foundation of China (No. U23A20595) and the Science and Technology Project of CNPC (No. 2023ZZ21). Z.W. acknowledges financial support from the China Scholarship Council (CSC) under Grant No. 202506050072. All data in this work are available upon request (chaozhong.qin@gmail.com)

Supplementary materials

Supplementary material associated with this article can be found, in the online version, at doi:10.1016/j.advwatres.2026.105531.

Appendix A. SliceGAN construction model validation

To construct REV-scale shale digital rocks, we employed the SliceGAN framework of KenchCooper (2021), a GAN-based method for generating 3D structures from 2D image slices. In this study, SliceGAN was applied to both REV-scale shale matrix images and individual OM/clay elements, thereby supplementing the limited availability of FIB-SEM data and enabling sub-rock-scale connectivity analysis. As illustrated in Fig. A1, the model consists of a 3D generator and three 2D discriminators based on a WGAN-GP architecture. During training, the generated 3D volume is sliced along three orthogonal directions and compared with the corresponding 2D training images.

The training of the 2D-to-3D construction models for OM, clay minerals, and REV-scale shale digital rocks was performed on a workstation equipped with an AMD EPYC 9754 CPU, 60 GB of RAM, and an NVIDIA RTX 4090 GPU. Each model was trained for approximately 50 epochs, requiring about 8 h of computation per sample.

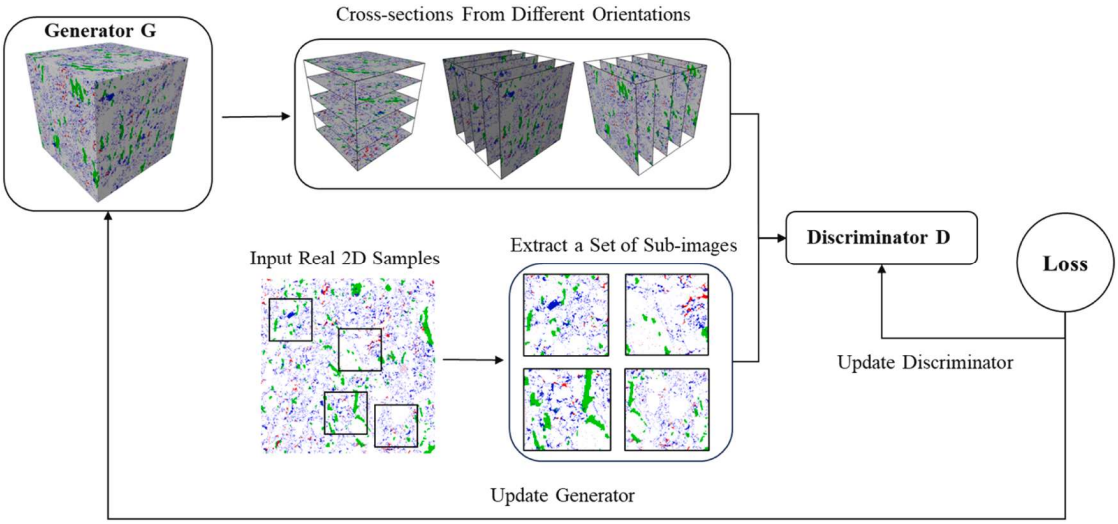


Fig. A1. Schematic illustration of the SliceGAN-based construction process for shale digital rocks.

To evaluate the reliability of SliceGAN construction, a validation test was conducted using FIB-SEM data with known 3D structures. A subvolume containing only organic matter and pores was extracted from the original FIB-SEM dataset and segmented. A representative 2D slice from the middle of this subvolume was used as the training image for SliceGAN. After training, the generated 3D structure was compared with the corresponding FIB-SEM reconstruction in terms of pore morphology, pore-size distribution, porosity, mean pore diameter, and coordination number. The selected FIB-SEM subvolume did not exhibit obvious directional anisotropy within the OM element, supporting the use of 2D image information for SliceGAN-based 3D construction.

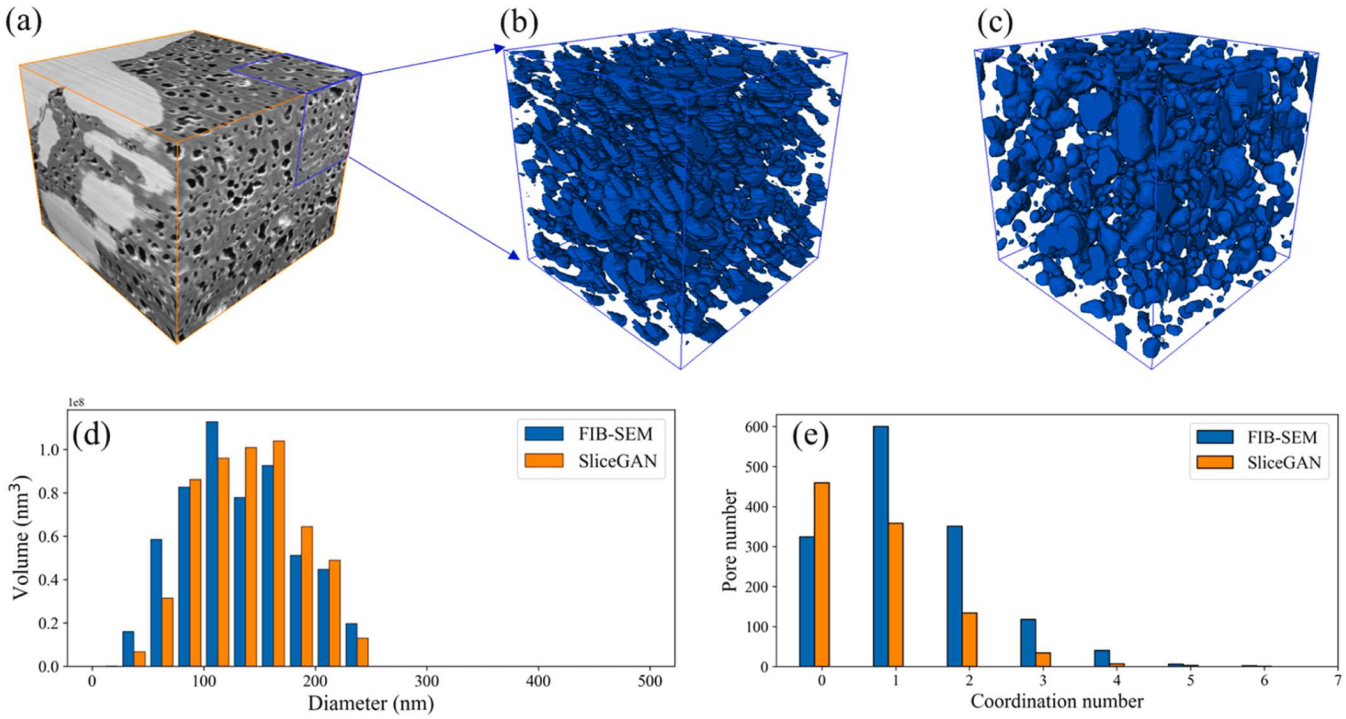


Fig. A2. Comparison between FIB-SEM and SliceGAN construction results. (a) Original FIB-SEM image; (b) 3D reconstruction of the selected FIB-SEM subregion; (c) 3D ronstruction generated by SliceGAN; (d) Comparison of pore size distributions between FIB-SEM and SliceGAN reconstructions; (e) Comparison of pore coordination number distributions between FIB-SEM and SliceGAN reconstructions.

As shown in Fig. A2, the SliceGAN-generated structure captures the main pore morphology of the FIB-SEM reconstruction. The pore-size distributions of the two reconstructions are highly consistent, and their coordination number distributions also show similar trends. Quantitatively, the porosity of the FIB-SEM reconstruction is 15.63%, whereas that of the SliceGAN construction is 15.73%, with a relative error of <3%. The average coordination number and mean pore diameter obtained from both methods also show good agreement (Table A1). These results indicate that SliceGAN can provide reliable 3D digital rock constructions for shale OM elements and can reasonably reproduce their pore-structure characteristics.

Table A1
Comparison of pore structure characteristics between FIB-SEM and SliceGAN reconstructions.

Reconstruction Method	Porosity (%)	Average Coordination Number	Average Pore Diameter (nm)
FIB-SEM	15.63	1.28	72.17
SliceGAN	15.73	0.94	79.03

Appendix B. Shale samples and basic characterization

Twelve shale cores were collected from various depths of Well H in the Wufeng–Longmaxi Formation (as shown in Table B1), located in the Luzhou Block of the Sichuan Basin, China. Among them, two cores were taken from the Wufeng Formation and ten from the Longmaxi Formation.

Table B1
Characteristics of the mineral composition and organic carbon content of samples.

Sample Number	Depth	TOC	Porosity	Permeability	Lithofacies	Mineral content (%)						
	(m)	(%)	(%)	(nD)		Quartz	Clay	Calcite	Dolomite	Feldspar	Pyrite	Other
H1	4102.27	2.09	3.61	37.73	Mixed shale	26.60	38.68	13.36	8.00	10.85	2.03	0.47
H2	4105.64	2.76	3.62	37.16	Mixed shale	18.21	33.95	14.56	23.61	7.46	1.95	0.25
H3	4106.58	2.11	4.16	49.84	Mixed shale	25.55	39.48	11.11	9.14	10.86	3.53	0.33
H4	4109.49	3.15	4.90	49.00	Mixed shale	32.87	48.28	1.93	1.20	12.85	2.68	0.17
H5	4111.96	2.44	4.67	47.98	Mixed shale	33.28	44.01	3.23	2.60	12.76	3.84	0.26
H6	4144.35	4.11	3.12	31.52	Siliceous shale	81.67	4.23	2.58	4.06	4.92	2.34	0.20
H7	4146.42	4.53	3.47	29.18	Siliceous shale	55.30	12.94	9.80	11.04	6.27	4.30	0.34
H8	4149.27	4.01	3.66	46.44	Siliceous shale	69.83	3.65	9.15	12.53	2.54	2.19	0.11
H9	4151.25	3.95	3.95	28.21	Siliceous shale	66.28	5.00	6.35	16.46	3.88	1.86	0.16
H10	4151.48	3.93	3.13	30.19	Siliceous shale	56.93	10.88	9.20	14.02	5.15	3.51	0.31
H11	4152.45	4.33	3.69	48.79	Calcareous shale	24.83	15.38	33.12	18.56	4.76	3.05	0.30
H12	4154.77	1.63	3.43	36.09	Siliceous shale	65.25	17.18	0.98	2.97	12.09	0.95	0.58

As shown in Table B1, the total organic carbon (TOC) contents of the twelve shale samples range from 1.63% to 4.53%. Lithofacies classification was conducted following the approach of Wang et al. (2017). The classification distinguishes siliceous, calcareous, and mixed shales according to the relative contents of minerals, with thresholds of roughly >50% for the dominant component and 30~50% for mixed compositions. Vertically, the shales near the Wufeng Formation contain higher proportions of feldspar and quartz and are dominated by siliceous lithofacies, whereas the upper intervals exhibit higher clay mineral contents and mainly consist of mixed shale.

Data availability

Data will be made available on request.

References

Alafnan, S., 2024. Hydrogen geostorage in organic-rich shales: critical insights into the role of cushion gas in hydrogen accumulation within organic nanoporous systems. SPE J. 29, 4471–4485. https://doi.org/10.2118/221468-PA.

Arganda-Carreras, I., Kaynig, V., Rueden, C., Eliceiri, K.W., Schindelin, J., Cardona, A., Sebastian Seung, H., 2017. Trainable Weka segmentation: a machine learning tool for microscopy pixel classification. Bioinformatics 33 (15), 2424–2426. https://doi.org/10.1093/bioinformatics/btx180.

Beskok, A., Karniadakis, G.E., 1999. A model for flows in channels, pipes, and ducts at micro and nano scales. Microscale Thermophys. Eng. 3 (1), 43–78.

Beucher, S., and Lantuéjoul, C. (1979). *Use of Watersheds in Contour Detection* (Vol. 132).

Cao, G., Lin, M., Ji, L., Jiang, W., Yang, M., 2019. Characterization of pore structures and gas transport characteristics of Longmaxi shale. Fuel 258, 116146. https://doi.org/10.1016/j.fuel.2019.116146.

Chen, F., Mehana, M., Nasrabadi, H., 2023. Molecular simulation of hydrogen-shale gas system phase behavior under multiscale conditions: a molecular-level analysis of hydrogen storage in shale gas reservoirs. Energy Fuels 37 (3), 2449–2456. https://doi.org/10.1021/acs.energyfuels.2c03571.

Chen, J., Jia, L., Zhang, J., Feng, Y., 2025. Super-resolution for electron microscope scanning images of shale via spatial-spectral domain attention network. Nat. Gas Ind. B 12, 147–157. https://doi.org/10.1016/j.ngib.2025.03.010.

Cui, X., Bustin, A., Bustin, R., 2009. Measurements of gas permeability and diffusivity of tight reservoir rocks: different approaches and their applications. Geofluids 9, 208–223. https://doi.org/10.1111/j.1468-8123.2009.00244.x.

Fan, Y., Liu, K., Yu, L., Liu, J., Regenauer-Lieb, K., 2022. Assessment of multi-scale pore structures and pore connectivity domains of marine shales by fractal dimensions and correlation lengths. Fuel 330, 125463. https://doi.org/10.1016/j.fuel.2022.125463.

Feng, J., Xiong, Q., Qu, Y., Yang, D., 2024. A new dual-scale pore network model with triple-pores for shale gas simulation. Geoenergy Sci. Eng. 235, 212710. https://doi.org/10.1016/j.geoen.2024.212710.

Gao, Z., Bai, L., Hu, Q.-H., Yang, Z., Jiang, Z., Wang, Z., Xin, H., Zhang, L., Yang, A., Jia, L., Liu, Z., Ma, G., 2024. Shale oil migration across multiple scales: a review of characterization methods and different patterns. Earth Sci. Rev. 254, 104819. https://doi.org/10.1016/j.earscirev.2024.104819.

Gostick, J., Khan, Z.A., Tranter, T.G., Kok, M.D.R., Agnaou, M., Sadeghi, M.A., Jervis, R., 2019. PoreSpy: a python toolkit for quantitative analysis of porous media images. J. Open. Source Softw. 4 (37), 1296. https://doi.org/10.21105/joss.01296.

Gou, Q., Xu, S., Hao, F., Yang, F., Zhang, B., Shu, Z., Zhang, A., Wang, Y., Lu, Y., Cheng, X., Qing, J., Gao, M., 2019. Full-scale pores and micro-fractures characterization using FE-SEM, gas adsorption, nano-CT and micro-CT: a case study of the Silurian Longmaxi formation shale in the Fuling area, Sichuan Basin, China. Fuel 253, 167–179. https://doi.org/10.1016/j.fuel.2019.04.116.

Guo, B., Ma, L., Tchelepi, H., 2018. Image-based micro-continuum model for gas flow in organic-rich shale rock. Adv. Water Resour. 122, 70–84. https://doi.org/10.1016/j.advwatres.2018.10.004.

Guo, X., Hu, D., Li, Y., Wei, Z., Wei, X., Liu, Z., 2017. Geological factors controlling shale gas enrichment and high production in Fuling shale gas field. Pet. Explor. Dev. 44 (4), 513–523. https://doi.org/10.1016/s1876-3804(17)30060-5.

Jiang, W., Ji, L., Luo, C., Lin, M., Cao, G., Hao, F., Chen, Z., He, Y., 2023. An optimization method for equivalent bulk permeability of gas shale matrix with crushed samples and re-recognition of the influence of pressure and particle size. Mar. Pet. Geol. 156, 106455. https://doi.org/10.1016/j.marpetgeo.2023.106455.

Kench, S., Cooper, S.J., 2021. Generating three-dimensional structures from a two-dimensional slice with generative adversarial network-based dimensionality expansion. Nat. Mach. Intell. 3 (4), 299–305. https://doi.org/10.1038/s42256-021-00322-1.

Kench, S., Squires, I., Dahari, A., Cooper, S.J., 2022. MicroLib: a library of 3D microstructures generated from 2D micrographs using SliceGAN. Sci. Data 9 (1). https://doi.org/10.1038/s41597-022-01744-1.

Li, Y., Wang, B., Xue, L., Liu, S., Wang, T., 2024. Shale mineral particles directional arrangement and its effect on the mesoscopic failure mechanism. Bull. Eng. Geol. Environ. 83 (1). https://doi.org/10.1007/s10064-023-03513-9.

Li, Y., Zhang, Z., Wei, S., Yang, P., Shang, Y., 2021. Opportunities in measuring multiscale pore structure of the continental shale of the Yanchang Formation, Ordos Basin, China. Energies 14 (17), 5282. https://doi.org/10.3390/en14175282. . *(Basel)*.

Liu, D., Yang, X., Zhang, D., Huang, S., Jiang, R., Rong, J., Wang, Z., Shi, B., Qin, C., 2025a. The pore-network-continuum hybrid modeling of nonlinear shale gas flow in digital rocks of organic matter. Phys. Fluids 37. https://doi.org/10.1063/5.0265700.

Liu, D., Yang, X., Zhao, S., Zhang, D., Huang, S., Zhu, N., Rong, J., Shi, B., Wang, Z., Qin, C., 2025b. Three-dimensional reconstruction and connectivity analysis of REV-size organic matter in shales. Front. Earth. Sci. 13. https://doi.org/10.3389/feart.2025.1537217 *(Lausanne)*.

Loucks, R.G., Reed, R.M., Ruppel, S.C., Hammes, U., 2012. Spectrum of pore types and networks in mudrocks and a descriptive classification for matrix-related mudrock pores. Am. Assoc. Pet. Geol. Bull. 96 (6), 1071–1098. https://doi.org/10.1306/08171111061.

Ma, C., Zhao, X., Wen, Z., He, Z., Jin, F., Guo, B., Chen, R., Zheng, J., Yang, G., Fan, X., Zhu, H., 2023. Multi-scale and multi-dimensional imaging of mineral matrix pore-fracture networks in lower-thermal-maturity lacustrine shale: examples from the paleogene Shahejie formation, Bohai Bay Basin. Energy Fuels 37 (15), 11125–11141. https://doi.org/10.1021/acs.energyfuels.3c01864.

Ma, L., Dowey, P.J., Rutter, E., Taylor, K.G., Lee, P.D., 2019. A novel upscaling procedure for characterising heterogeneous shale porosity from nanometer-to millimetre-scale in 3D. Energy 181, 1285–1297. https://doi.org/10.1016/j.energy.2019.06.011.

Ma, L., Fauchille, A.-L., Ansari, H., Chandler, M., Ashby, P., Taylor, K., Pini, R., Lee, P.D., 2021. Linking multi-scale 3D microstructure to potential enhanced natural gas recovery and subsurface CO_2 storage for Bowland shale, UK. Energy Environ. Sci. 14 (8), 4481–4498. https://doi.org/10.1039/d0ee03651j.

Ma, L., Slater, T., Dowey, P.J., Yue, S., Rutter, E.H., Taylor, K.G., Lee, P.D., 2018. Hierarchical integration of porosity in shales. Sci. Rep. 8 (1), 11683. https://doi.org/10.1038/s41598-018-30153-x.

Qin, X., Wang, H., Xia, Y., He, W., Xia, X., Cai, J., 2024. Three-dimensional modeling of nanoconfined multiphase flow in clay nanopores using FIB-SEM images of shale. Innov. Energy 1, 100050. https://doi.org/10.59717/j.xinn-energy.2024.100050.

Rexer, T., Mathia, E., Aplin, A., Thomas, K., 2014. High-pressure methane adsorption and characterization of pores in posidonia shales and isolated kerogens. Energy Fuels 28, 2886–2901. https://doi.org/10.1021/ef402466m.

Shi, B., Jiang, H., Guo, B., Tian, J., Qin, C., 2024. Modeling of flow and transport in multiscale digital rocks aided by grid coarsening of microporous domains. J. Hydrol. 633, 131003. https://doi.org/10.1016/j.jhydrol.2024.131003.

Shi, B., Rong, J., Jiang, H., Guo, B., Hassanizadeh, S.M., Qin, C.-Z., 2025. The pore-network-continuum modeling of two-phase flow properties for multiscale digital rocks. Adv. Water Resour. 206, 105138. https://doi.org/10.1016/j.advwatres.2025.105138.

Wang, C., Zhao, Y., Wu, R., Bi, J., Zhang, K., 2024a. Shale reservoir storage of hydrogen: adsorption and diffusion on shale. Fuel 357, 129919. https://doi.org/10.1016/j.fuel.2023.129919.

Wang, P., Jiang, Z., Chen, L., Yin, L., Li, Z., Zhang, C., Tang, X., Wang, G., 2016. Pore structure characterization for the Longmaxi and Niutitang shales in the Upper Yangtze Platform, South China: evidence from focused ion beam–He ion microscopy, nano-computerized tomography and gas adsorption analysis. Mar. Pet. Geol. 77, 1323–1337. https://doi.org/10.1016/j.marpetgeo.2016.09.001.

Wang, P., Jiang, Z., Yin, L., Chen, L., Li, Z., Zhang, C., Li, T., Huang, P., 2017. Lithofacies classification and its effect on pore structure of the Cambrian marine shale in the Upper Yangtze Platform, South China: evidence from FE-SEM and gas adsorption analysis. J. Pet. Sci. Eng. 156, 307–321. https://doi.org/10.1016/j.petrol.2017.06.011.

Wang, Q., Wang, T., Liu, W., Zhang, J., Feng, Q., Lu, H., Peng, P.A., 2019. Relationships among composition, porosity and permeability of Longmaxi shale reservoir in the Weiyuan Block, Sichuan Basin, China. Mar. Pet. Geol. 102, 33–47. https://doi.org/10.1016/j.marpetgeo.2018.12.026.

Wang, T.-Y., Tian, S.-C., Liu, Q.-L., Li, G.-S., Sheng, M., Ren, W.-X., Zhang, P.-P., 2021. Pore structure characterization and its effect on methane adsorption in shale kerogen. Pet. Sci. 18 (2), 565–578. https://doi.org/10.1007/s12182-020-00528-9.

Wang, Y., Sun, Q., Chen, F., Wang, M., 2024b. Multiscale model for hydrogen transport and storage in shale reservoirs. SPE J. 29, 3238–3264. https://doi.org/10.2118/219472-PA.

Wei, J., Zhou, X., Shamil, S., Yuriy, K., Yang, E., Yang, Y., Wang, A., 2023. Lithofacies influence characteristics on typical shale pore structure. Energy 282, 128728. https://doi.org/10.1016/j.energy.2023.128728.

Wu, J., Luo, C., Zhong, K., Li, Y., Li, G., Du, Z., Yang, J., 2023a. Innovative characterization of organic nanopores in marine shale by the integration of HIM and SEM. Energy 282, 128390. https://doi.org/10.1016/j.energy.2023.128390.

Wu, Y., An, S., Tahmasebi, P., Liu, K., Lin, C., Kamrava, S., Liu, C., Yu, C., Zhang, T., Sun, S., Krevor, S., Niasar, V., 2023b. An end-to-end approach to predict physical properties of heterogeneous porous media: coupling deep learning and physics-based features. Fuel 352, 128753. https://doi.org/10.1016/j.fuel.2023.128753.

Zhang, T., Ellis, G., Ruppel, S., Milliken, K., Yang, R., 2012. Effect of organic-matter type and thermal maturity on methane adsoption in shale-gas systems. Org. Geochem. 47, 120–131. https://doi.org/10.1016/j.orggeochem.2012.03.012.

Zhang, T., Li, D.Y., Lu, F.F., 2021. A pore space reconstruction method of shale based on autoencoders and generative adversarial networks. Comput. Geosci. 25 (6), 2149–2165. https://doi.org/10.1007/s10596-021-10083-w.
Zhao, J.Y., Wang, F.Y., Cai, J.C., 2021. 3D tight sandstone digital rock reconstruction with deep learning. J. Pet. Sci. Eng. 207, 109020. https://doi.org/10.1016/j.petrol.2021.109020.
Zhao, X., Shi, B., Wang, X., Zhao, J., Jiang, F., Qin, C.-Z., 2025. Modeling of permeability and formation factor of carbonate digital rocks: dual-pore-network and pore-network-continuum models. Transp. Porous. Media 152 (6). https://doi.org/10.1007/s11242-025-02177-1.